J Mater Sci (2025) 60:4258–4278

Composites & nanocomposites

A comprehensive investigation of PtNPs/PEI N-GQDs nanocomposite: DFT modeling, anticancer activity, and biosensing applications

Buket Altinok Gunes[1,*], Omer Faruk Kirlangic[1], Murat Kilic[1], Didem Ketenoglu[2], Aysenur Aslan[1], Sultan Yagmur Kabas[3], Afsar Kabas[4], Ismet Kaya[5], Asuman Sunguroglu[6], Nadide Ors Yildirim[7], Taner Ozgurtas[8], Ecem Kaya Sezginer[9], Bahadir Boyacioglu[1], Huseyin Unver[10], and Mustafa Yildiz[5,*]

[1] *Vocational School of Health Services, Ankara University, 06290 Ankara, Turkey*
[2] *Department of Physics Engineering, Faculty of Engineering, Ankara University, 06100 Ankara, Turkey*
[3] *Lapseki Vocational School, Department of Chemistry and Chemical Processing Technologies, Çanakkale Onsekiz Mart University, 17800 Çanakkale, Turkey*
[4] *Department of Physics, Faculty of Science, Canakkale Onsekiz Mart University, 17100 Canakkale, Turkey*
[5] *Department of Chemistry, Faculty of Science, Çanakkale Onsekiz Mart University, 17020 Çanakkale, Turkey*
[6] *Department of Medical Biology, School of Medicine, Ankara University, 06230 Ankara, Turkey*
[7] *Department of Anesthesiology and Reanimation, Gulhane School of Medicine, University of Health Science, 06010 Ankara, Turkey*
[8] *Department of Medical Biochemistry, Gulhane School of Medicine, University of Health Science, 06010 Ankara, Turkey*
[9] *Department of Biochemistry, Faculty of Pharmacy, Ankara University, 06100 Ankara, Turkey*
[10] *Department of Physics, Faculty of Science, Ankara University, 06100 Ankara, Turkey*

Received: 1 August 2024
Accepted: 9 February 2025
Published online: 24 February 2025

ABSTRACT

This research focuses on the synthesis and characterization of a novel nanocomposite, PtNPs/PEI N-GQDs, utilizing FTIR, UV–Vis, SEM, TEM, XPS, and XRD techniques. The study investigates the cytotoxic, apoptotic, and antiangiogenic effects of the nanocomposite on OVCAR-3 cells, aiming to understand the interplay between nanomaterials and cancer. Additionally, the electrochemical properties of PtNPs/PEI N-GQDs-modified glassy carbon electrodes (GCE) are explored, emphasizing analyses of HOMO–LUMO energy levels and band gap energy. Density Functional Theory (DFT) analysis results further support these findings by providing insights into the electronic structure and energetics of the nanocomposite. The nanocomposite exhibits promising electrochemical behavior, demonstrating high capacitance and sensitivity in glucose detection through cyclic voltammetry (CV) and differential pulse voltammetry (DPV) techniques. Selectivity towards glucose among interfering bioanalytes is highlighted, showcasing potential applications in tumor monitoring and diagnosis. Furthermore, the nanocomposite displays significant toxicity against cancer cells, inducing apoptosis and cell cycle arrest. Antiangiogenic effects are also observed,

Handling Editor: Subha Narayan Rath.

Address correspondence to E-mail: baltinok@ankara.edu.tr; myildiz@comu.edu.tr

https://doi.org/10.1007/s10853-025-10722-y

suggesting potential therapeutic benefits. Overall, these findings underscore the multifunctional properties of the synthesized nanocomposite, offering insights into its potential for cancer therapy and biosensor applications for glucose detection in bodily fluids.

GRAPHICAL ABSTRACT

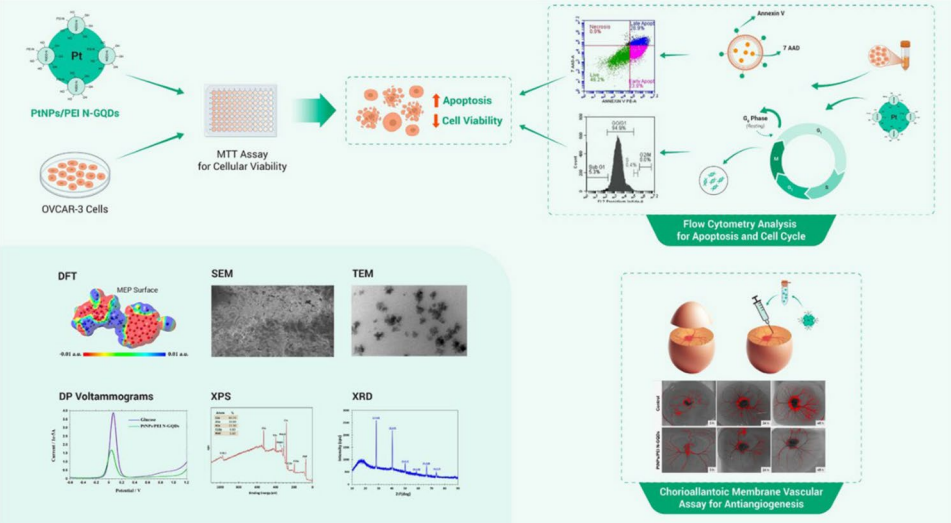

Introduction

Graphene quantum dots (GQDs) are renowned for their unique properties. Doping GQDs with heteroatoms is an effective strategy to fine-tune their intrinsic properties, thereby discovering new phenomena that enhance device performance. This modification of surface, electronic, and local chemical properties of carbon nanomaterials via heteroatom doping is highly effective [1–3]. Nitrogen is often chosen for doping due to its similar atomic size and bonding ability with carbon atoms, which can effectively control the band gap of graphene and impart new properties for various applications [1, 4–7].

Nitrogen-doped graphene (N-G) and nitrogen-doped graphene quantum dots (N-GQDs) can form composites with a variety of materials, including metals, metal oxides, nitrides, polymers, and semiconductors. These composites demonstrate enhanced functionality and superior performance in supercapacitors, batteries, sensors, fuel cells, solar cells, and photocatalysts, showcasing the versatility and potential of N-G and N-GQDs in technological advancements [8–10]. PEI-functionalized GQDs were used to remove Cd^{2+} ions from wastewater, and it was shown that the material showed ultra-high adsorption capacity and GQDs-PEI can be easily regenerated [11]. Again, polyethylenimine-modified graphene quantum dots were found to promote endothelial cell proliferation [12]. However, these compounds (PEI N-GQDs) were obtained in multiple steps, which is different from our synthesis method, the green method in one step in one pot. Therefore, the formulations of the compounds are also different.

Beyond their environmental applications, it has been shown in the literature that PEI-functionalized graphene quantum dots (GQDs) exhibit low toxicity and do not cause cellular damage at low concentrations. Xu et al. [12] reported that PEI-modified GQDs promoted endothelial cell proliferation without adversely affecting cell viability, suggesting their low toxicity and good biocompatibility. Similarly, Gunes et al. [13] demonstrated that PEI-functionalized nitrogen-doped GQDs did not cause significant cytotoxicity at low concentrations in human ovarian cancer cells. The study highlights that PEI-functionalized N-GQDs exhibit potential therapeutic effects by maintaining their biocompatibility and can be safely used in biological applications. The review by Biswas et al. [14] reveals that GQDs, including PEI-functionalized variants, are less toxic compared to conventional quantum

dots and thus are promising candidates in bioimaging and drug delivery. This finding is also in agreement with the study of Wang et al. [15], who stated that GQDs have low cytotoxicity and good biocompatibility. Lo et al. [16] showed that the bioavailability of GQDs increased with the use of biopolymers such as PEI, which contributed to their biocompatibility and low toxicity. Furthermore, Raghavan's study [17] confirms that nitrogen-doped GQDs exhibit non-haemolytic properties and are compatible with red blood cells.

GQDs have garnered significant attention due to their remarkable physicochemical properties, ease of synthesis, and compatibility with various materials. These attributes make them excellent frameworks for electrochemical sensing. Recent reviews have highlighted advancements in GQD-based nanocomposites for electrochemical sensors and biosensors, focusing on fabrication methods and applications in detecting environmental, medical, and agricultural analytes [18]. Nitrogen-doped graphene quantum dots (N-GQDs) exhibit a smaller band gap energy compared to other modified electrodes, enhancing electrochemical oxidation capability and electron transfer efficiency [19].

Glucose detection is critical for diabetes management, necessitating sensitive determination by electrochemical methods. Surface modification with catalysts is essential, as glassy carbon electrodes (GCE) are not suitable for direct glucose oxidation [20]. The importance of maintaining specific glucose levels has driven the increased use of graphene sensors for glucose monitoring. Developments in laser-induced graphene sensors for electrochemical glucose detection have been reviewed, highlighting the promise of acidic oxygen-based functional groups in GQDs as solid-state and solution electrolytes for supercapacitors. Neutralizing these acidic groups with potassium hydroxide significantly increases ionic conductivity and ion-donating ability [21, 22]. Composite materials containing heteroatom doping or other electrochemically active materials are employed to address the aggregation of graphene sheets, which negatively affects energy storage performance [23].

N-GQDs are typically synthesized via one-pot, one-step hydrothermal reactions using citric acid and urea or primary amines [24–36]. Their photoluminescence (PL) is influenced by heteroatom doping with elements such as oxygen, nitrogen, boron, sulfur, and phosphorus [37–40], which can alter the energy gap between HOMOs and LUMOs [41]. Electron-accepting impurities widen this gap, while electron-donating impurities narrow it. Nitrogen doping generally results in a red shift in PL and improved quantum efficiency. Beyond sensing, GQDs are being developed for drug delivery systems. Due to the combined properties of graphene and quantum dots, they hold potential as nanomedical drug delivery systems (NDDS) for cancer treatment [42]. Given the increasing incidence and mortality of cancer, especially ovarian cancer, less invasive and more effective treatments are needed. Traditional treatments such as chemotherapy, radiation, and surgery have limitations, making it important to develop more effective and less disruptive treatments [43, 44].

In this study, a PtNPs/PEI N-GQD nanocomposite was synthesized and characterized. The electrochemical properties of this nanocomposite-modified GCE were examined, revealing the HOMO–LUMO energy levels, band gap energy, and specific capacitance. The research also explored the glucose detection capabilities of the nanocomposite. Additionally, the anticancer effects on OVCAR-3 ovarian cancer cells and the compound's ability to inhibit angiogenesis using the ex ovo chorioallantoic membrane (CAM) assay were investigated [45].

Materials and methods

Materials

Various analytical methods, similar to those in our previous research [13], were used to characterize the PtNPs/PEI N-GQDs nanocomposite. Fourier Transform Infrared Spectrsocopy (FTIR) and UV–Visible spectra were recorded, TEM was used for morphological analysis, X-ray photoelectron spectroscopy (XPS) for elemental composition, and X-ray diffraction (XRD) for structural analysis. Chemicals were sourced from Sigma-Aldrich without further purification.

Synthesis of PtNPs/ PEI N-GQDs nanocomposite

Following the synthesis method in our previous research [13], PEI N-GQDs [32–36] were mixed with water and combined with a K_2PtCl_4 solution. The mixture was heated at 90 °C for 2 h, resulting in a color change from yellow to gray-black, indicating the formation of the PtNPs/PEI N-GQD nanocomposite.

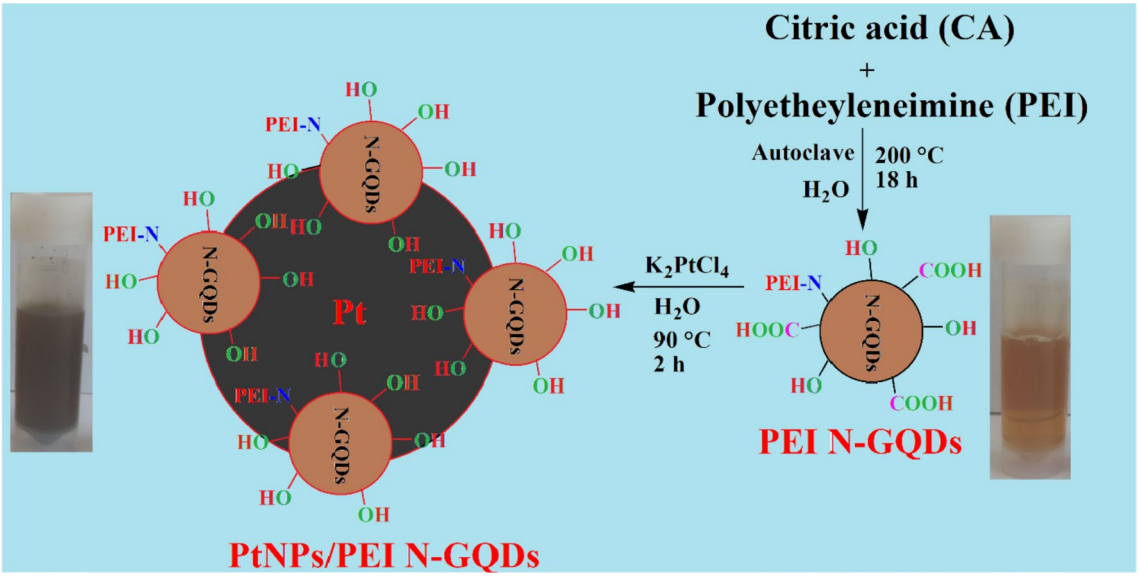

Scheme 1 Synthesis of PtNPs/PEI N-doped GQDs nanocomposite

The solution was then filtered, washed with deionized water, dried in a vacuum oven, and stored in a desiccator.

Electrochemical measurements

Electrochemical measurements, following methods similar to those in [46], were conducted using a CHI660D CH Instruments Electrochemical Workstation. Cyclic voltammetry (CV) and differential pulse voltammetry (DPV) were performed with a glassy carbon electrode (GCE), an Ag/AgCl reference electrode, and a platinum wire counter electrode. The GCE was modified with PtNPs/PEI N-GQDs nanocomposite and recoated with PtNPs/PEI N-GQDs before measurements. Experiments used a 0.1 M KCl solution (pH 7.0) containing 50 μM $K_3Fe(CN)_6$ and $K_4Fe(CN)_6$, within a potential range of − 0.8 to + 1.2 V. DPV parameters included a pulse amplitude of 50 mV and pulse time of 0.04 s, while CV analysis employed scan rates from 5 mV/s to 200 mV/s.

DFT method

This section provides an in-depth analysis of PtNPs/PEI N-GQDs, building on previous studies [13, 36]. The focus is on evaluating the sensitivity and selectivity of these materials by exploring their electronic properties. Key analyses include geometry optimization, electronic structure assessment, charge distribution studies, and vibrational property examination. These are essential for understanding the nanocomposites' electronic, structural, thermal, and energetic aspects, with implications for electrochemistry, glucose biosensing, and cancer cell studies (Scheme 1).

The theoretical model integrates PtNPs into the PEI N-GQDs structure, as shown in Scheme 2. Density Functional Theory (DFT) calculations were performed using the B3LYP functional and Lanl2dz basis set [47, 48] within Gaussian 09W [49]. Structures were visualized with GaussView 5.0 [50] to evaluate structural and spectroscopic properties. Additional analyses included Fourier Transform Infrared (FTIR) spectra for molecular vibrations and determining properties such as HOMO, LUMO, MEP, and HOMO–LUMO energy gap. Density of State (DOS) plots were created with Gauss-Sum v3.0 [51], and UV–Vis data were obtained through Time-Dependent Density Functional Theory (TD-DFT) calculations [52] to study electronic transitions and optical properties.

Cell culture

The human ovarian carcinoma (OVCAR-3) cell line was grown in RPMI-1640 medium supplemented with L-glutamine (Bio-Ind, USA), 20% fetal bovine serum (Bio-Ind, USA), 100 U/mL penicillin, and 100 mg/mL streptomycin (Gibco/USA) at 37 °C in 5% CO2 and 95% humidity [13, 53]. OVCAR-3 cells were obtained

Scheme 2 Theoretical model of PtNPs/PEI N-doped GQDs nanocomposite

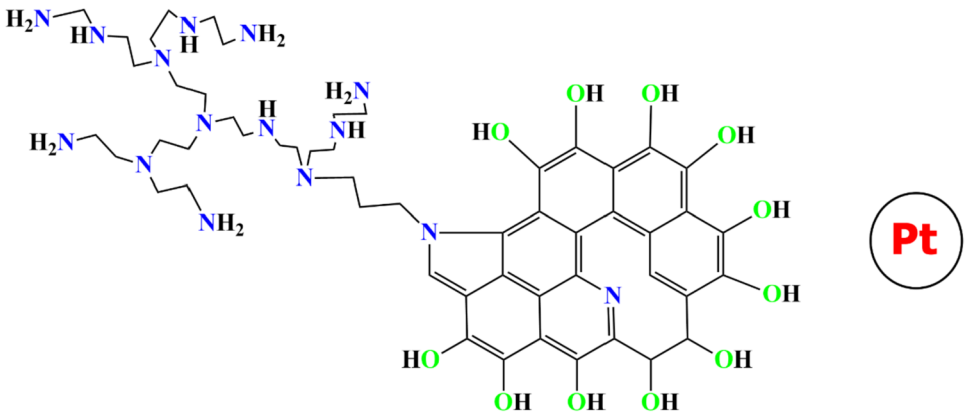

from the American Type Culture Collection (ATCC, Rockville, MD, USA).

Cell viability test

OVCAR-3 cells (1×10^4 cells/well) were seeded in 96-well plates for 24 and 48 h, and PtNPs/PEI N-GQDs nanocomposites were added to the cells at 12 varying concentrations, each halved from a minimum of 0.24 µg/µL to a maximum of 500 µg/µL. After 24 and 48 h of treatment with the nanocomposite, the MTT (3-[4,5-dimethylthiazol-2-yl]-2,5 diphenyl tetrazolium bromide) assay (Sigma, USA) was used to determine the proliferation of the cells. 10 µL of MTT reagent (5 mg/ml) was added to each well and incubated for 4 h at 37 °C. After 4 h, 100 µL of isopropanol was added to each well plate. The optical density of each experiment was measured using a spectrophotometric plate reader (Biotek, USA). At 550 nm to 690 nm, the plate reader was adjusted.

Cell viability in untreated cells was taken to be 100%, and the percentage of cell viability in the treatment group was calculated correspondingly. Distilled water was used as a negative control and as a solvent for the nanocomposite. The nanocomposite and distilled water had a maximum concentration of 0.5% [13].

Flow cytometric analysis (Annexin V/7-AAD) for detecting apoptosis

OVCAR-3 cells (1×10^5 cells/well) were seeded in 24-well plates. The cells were treated with PtNPs/PEI N-GQDs nanocomposite for 48 h. After 48 h, cells were collected, washed twice with PBS, centrifuged, and resuspended in binding buffer (1XBB). PE Annexin V-PE (5 µL) and 7-AAD (5 µL) were added to 100 µL of cell suspension and incubated for 15 min at room temperature (BD Biosciences, USA). At the end of the incubation, 1X BB (400 µL) was added. Apoptosis was assessed by flow cytometry (BD Accuri C6 Flow Cytometer)[13, 53].

Cell cycle analysis

OVCAR-3 cells (1×10^5/well) were incubated for 48 h in a medium containing PtNPs/PEI N-GQDs nanocomposite and distilled water, then collected and resuspended in 75% ice-cold ethanol (Merck, Germany) at 4 °C overnight. The cells were then washed with 2X PBS. After washing, the cells were treated with RNase (Sigma, USA) (50 µg/mL) for 15 min at 37 °C and propidium iodide (PI) (Sigma, USA) (50 µg/mL) for 15 min at 4 °C without light. DNA content was analyzed by flow cytometry (BD Accuri C6 flow cytometer) [13, 53].

CAM Assay for angiogenesis

Ex ovo CAM assay was performed on fertilized chicken eggs that were cultured at 37 °C and 85–90% relative humidity. Fertilized chicken eggs were obtained from Atak-S chickens produced at the Poultry Research Institute, Ministry of Agriculture and Forestry, (Ankara, Turkey). The eggs were first cleaned of particles like feces, mud, and feathers from their exterior using a dry, soft tissue to try not to damage the shell, in accordance with the ex ovo CAM assay protocol [54]. The cleaned eggs were incubated in an incubator (CIMUKA 40080 serial number-incubator) for 72 h by rotating for 2 h. Incubation temperature and humidity of the incubator were kept stable during the study. After incubation, the eggs were observed

with a light source and the embryo side was labeled. Using forceps from the other side, the eggs were broken so that the chosen area stayed on top. The eggs taken into the weighing container were covered with glass lids sterilized with ethylene oxide and put back into the incubator. For three more days, the eggs were incubated to increase the visibility of the CAM. PtNPs/PEI N-GQDs nanocomposite were applied ex ovo to the chorioallantoic membrane following incubation. Sterilized filter papers with a diameter of 6 mm were utilized as carrier support material to keep the application to a specific area. Each filter paper, cut to an identical size, was dosed with 50 µL of PtNPs/PEI N-GQDs (10.05 µg/µL) nanocomposite solution. Following the application, the groups were observed at 0, 24, and 48 h using a stereomicroscope (S6D; Leica Microsystems, Heerbrugg, Switzerland). Quantitative analysis of the captured images was analyzed using the Image J program (National Institutes of Health, Bethesda, MD, USA) [55].

Statistics

All experiments were repeated three times in triplicate. All experimental data were presented as mean SD (standard deviation). GraphPad Prism statistical software was used to analyze the data. The control and treatment groups were compared using ANOVA analysis or t-tests, as appropriate. $p < 0.05$ and $p < 0.001$ were defined as statistically significant.

Results and discussion

Characterization of PtNPs/ PEI N-GQDs nanocomposite (FT-IR, UV–Vis, XRD, SEM, TEM and XPS)

The FT-IR spectrum of PtNPs/PEI N-GQDs nanocomposite reveals vibration bands corresponding to OH (3845–3737 cm^{-1}), NH_2 + NH (3421–3205 cm^{-1}), C-H (2948 cm^{-1}), C=N (1648 cm^{-1}), C=C (1587 cm^{-1}), C–N (1448 cm^{-1}), and C–O (1398 cm^{-1}) (Fig. S1). Comparison with the FT-IR spectrum of pure PEI N-GQDs shows a shift to higher frequencies in the functional groups of Pt metal nanocomposites, indicating oxidation of GQDs and reduction of metals.

The UV–vis absorbance spectra of PEI N-GQDs as well as those of PtNPs/PEI N-GQD nanocomposites (Fig. 1a) show a marked disparity in some of the

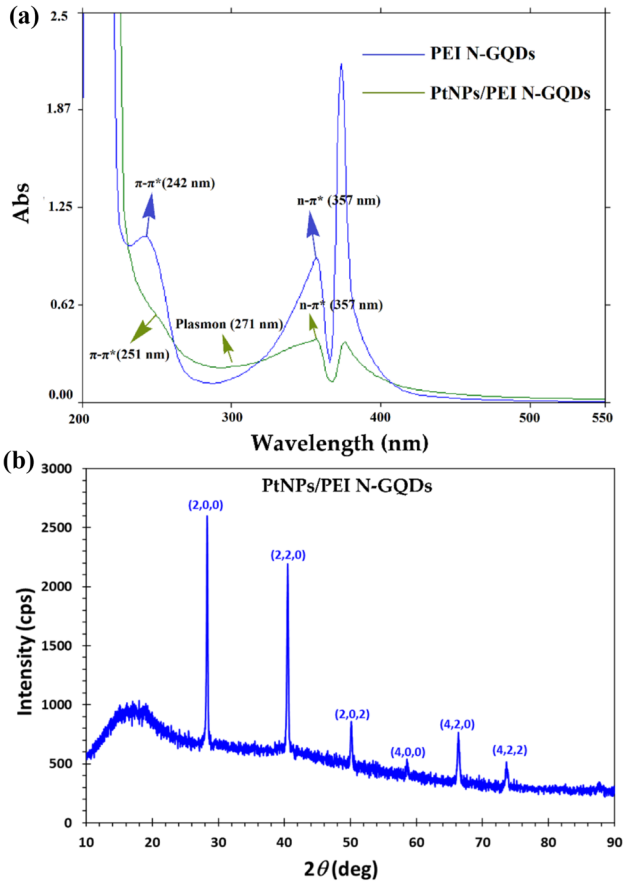

Figure 1 **a** Absorption spectra of the suspension PEI N-GQDs and PtNPs/PEI N-GQDs nanocomposite in water and **b** XRD pattern of PtNPs/PEI N-GQDs nanocomposite.

electronic and structural characteristics. Firstly, PEI N-GQDs shows the presence of a π-π* transition around 242 nm, which signifies the presence of aromatic C=C bonds, and a high-intensity n-π* transition at about 357 nm, which may be due to oxygen surface defects or nitrogen substitution. In the PtNPs/PEI N-GQDs nanocomposite, the π-π* transition occurs at 251 nm, indicating the presence of interfacial electronic interaction between PtNPs and N-GQDs. Furthermore, a characteristic plasmon resonance at 271 nm is consistent with the incorporation of PtNPs into the composite. Plasmonic nanoparticles (PtNPs) are incorporated into the PEI N-GQDs composite. Upon integration, they seem to lose their distinct physical characteristics and blend seamlessly with the composite. In the PtNPs/PEI N-GQDs nanocomposite, the decrease in the intensity of the n-π* transition at 357 nm indicates an electron transfer between PEI N-GQDs and PtNPs and also shows the synergism between these

materials. It is expected that the observed changes will help to improve the electron transfer properties of materials and their practical application in catalysis, biosensors systems, or other advanced materials that can help in increasing the optical bandgap behavior.

The XRD pattern of the PtNPs/PEI N-GQDs nanocomposite is shown in Fig. 1b. The curve for PtNPs/PEI N-GQDs exhibits distinct features: a broad peak centered at approximately 2θ = 17.10° and a narrower, more intense peak at 2θ = 28.28°. The broad peak around 17.10° corresponds to graphene samples and graphene nanosheets [56]. This sharp peak at about 28.8° (200) in the PtNPs/PEI N-GQDs crystal pattern suggests oxidation of COOH functional groups in PEI N-GQDs to OH and possibly further to quinone during Pt reduction [57], due to Pt's higher standard reduction potential compared to Pd.

This results in PEI N-GQDs with a more diverse array of side groups. Consequently, the structure of N-GQDs differs in Pd and Pt nanocomposites [13, 58]. Comparing with literature data [58], the PtNPs/PEI N-GQDs nanocomposite shows characteristic Pt peaks at 28.26°, 40.48°, 50.10°, 58.62°, 66.35°, and 73.65°, indexed as (2,0,0), (220), (202), (400), (420), and (422). According to the Bragg Eq. ($2d\sin\theta = \lambda$), the layer thickness calculated for PtNPs/PEI N-GQDs was 1.055 nm. Using the Scherrer formula [59], the average crystallite size was determined to be 5.60 nm for PEI N-GQDs and 39.90 nm for PtNPs. Consequently, the XRD peak profile of the PtNPs/PEI N-GQDs nanocomposite synthesized in this study illustrates significant characteristic peak profiles and plane reflectance indexing for Pt, reflecting variations within PEI N-GQDs due to metal-induced oxidation reactions [13].

The XPS spectrum (Fig. 2a) confirms carbon (283.39 eV), nitrogen (398.35 eV), oxygen (530.37 eV), and platinum (332.31 eV for Pt4d3, 314.31 eV for Pt4d5, 71.28 eV for Pt4f) in PtNPs/PEI N-GQDs nanocomposite. Cl impurities are observed at 267.25 eV (Cl2s) and 196.26 eV (Cl2p), with an oxygen Auger peak (O KL1) at 976.66 eV.

SEM and TEM images (Fig. 2b and c) illustrate relatively uniform layers and porous structures of PtNPs/PEI N-GQDs nanocomposite, with Pt particle sizes ranging from 7 to 16 nm. PEI N-doped GQDs maintain their spherical porous structures dispersed among Pt agglomerates. Overall, characterization techniques, including FT-IR, UV–Vis, XRD, XPS, SEM, and TEM confirm the structural properties and composition of

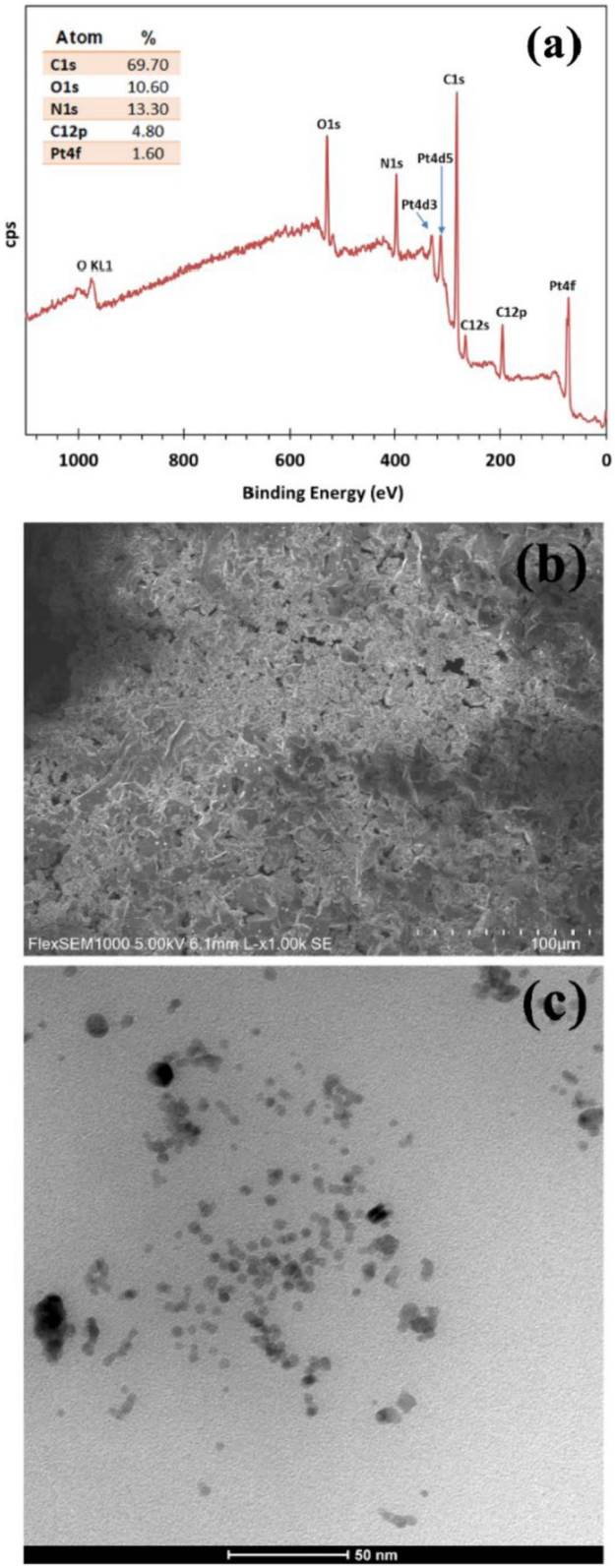

Figure 2 **a** XPS, **b** SEM and **c** TEM analyses of PtNPs/PEI N-GQDs nanocomposite.

PtNPs/PEI N-GQDs nanocomposite, highlighting its potential for various applications.

Electrochemical properties of PtNPs/PEI N-GQDs nanocomposite

Using similar methods described in reference [46], the electrochemical performance of GC and PtNPs/PEI N-GQDs nanocomposite-modified GC electrodes was investigated in 0.1 M KCl solution (pH 7) containing 50 µM $K_3Fe(CN)_6/K_4Fe(CN)_6$ at a scan rate of 100 mVs^{-1} (Fig. 3a). The PtNPs/PEI N-GQDs nanocomposite-modified electrode exhibited distinct oxidation and reduction peaks, while the unmodified GC electrode showed no redox peaks. Using cyclic voltammetry (CV), the HOMO, LUMO energy levels, and band gap energy (E_{gap}) [46, 60] of the PtNPs/PEI N-GQDs nanocomposite were calculated (Fig. 3a). The HOMO and LUMO energy levels were determined to be -5.163 eV and -4.991 eV, respectively, with a calculated band gap of 0.172 eV. The smaller HOMO–LUMO gap indicates higher reactivity, beneficial for biosensing applications. Scan rate effects on voltammograms were also examined (Fig. 3b), revealing peak shifts as scan rates increased, attributed to reduced electrolyte ion access to the electrode surface [61].

Specific capacitance (C_p) was determined using a modified approach [46] for PtNPs/PEI N-GQDs nanocomposite at scan rates ranging from 5 to 200 mVs^{-1} (Fig. 3c). C_p values ranged from 1.008 to 0.242 Fg^{-1}, with the highest value observed at a 5 mVs^{-1} scan rate, indicating superior capacitive behavior.

Sensitive detection of glucose

Electrochemical biosensors offer rapid and sensitive responses, enabling real-time monitoring and miniaturization suitable for implantation into living cells. However, these biosensors must provide sensitive detection within specific concentration ranges—typically 0.01–1 µM for healthy individuals and in the nanomolar range for those with health conditions. They also require selectivity to distinguish the target analyte from interfering biochemical ions and molecules oxidized within the same potential window [46].

The electrochemical responses of GC and PtNPs/PEI N-GQDs nanocomposite-modified GC electrodes were assessed in a 0.1 M KCl solution (pH 7) containing 50 µM $K_3Fe(CN)_6$ and $K_4Fe(CN)_6$, with 1 mM glucose. As depicted in Fig. 4a, while

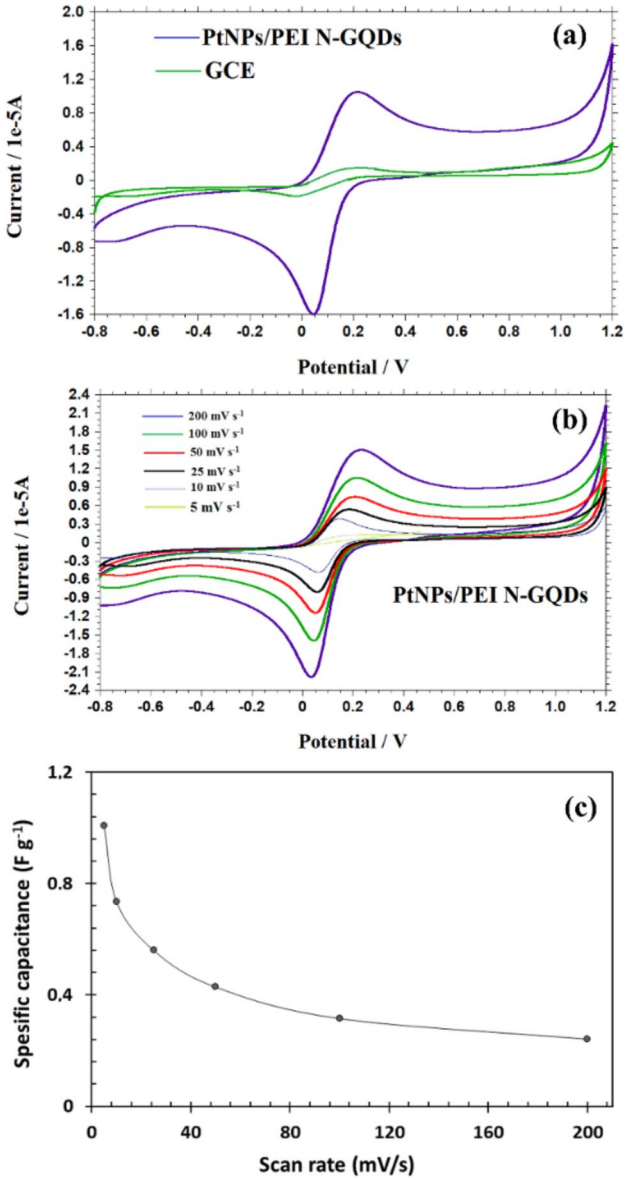

Figure 3 CV voltammograms of (**a**) both bare glassy carbon (GC) and PtNPs/PEI N-GQDs nanocomposite electrodes in 0.1 M KCl solution (pH: 7) containing 50 µM $K_3Fe(CN)_6$ and $K_4Fe(CN)_6$ at the scan rate 100 mVs^{-1}, **b** Cyclic voltammograms of PtNPs/PEI N-GQDs nanocomposite electrode in 0.1 M KCl containing 50 µM $K_3Fe(CN)_6$ and $K_4Fe(CN)_6$ at the verius scan rates (5–200 mVs^{-1}), and **c** specific capacitance values of the PtNPs/PEI N-GQDs nanocomposite at the scan rates of 5, 10, 20, 50, 100, and 200 mV s^{-1}.

oxidation and reduction peaks were observed at 0.340 V and -0.036 V, respectively, for the PtNPs/PEI N-GQDs nanocomposite-modified GC electrode, no such peaks were observed for the GC electrode

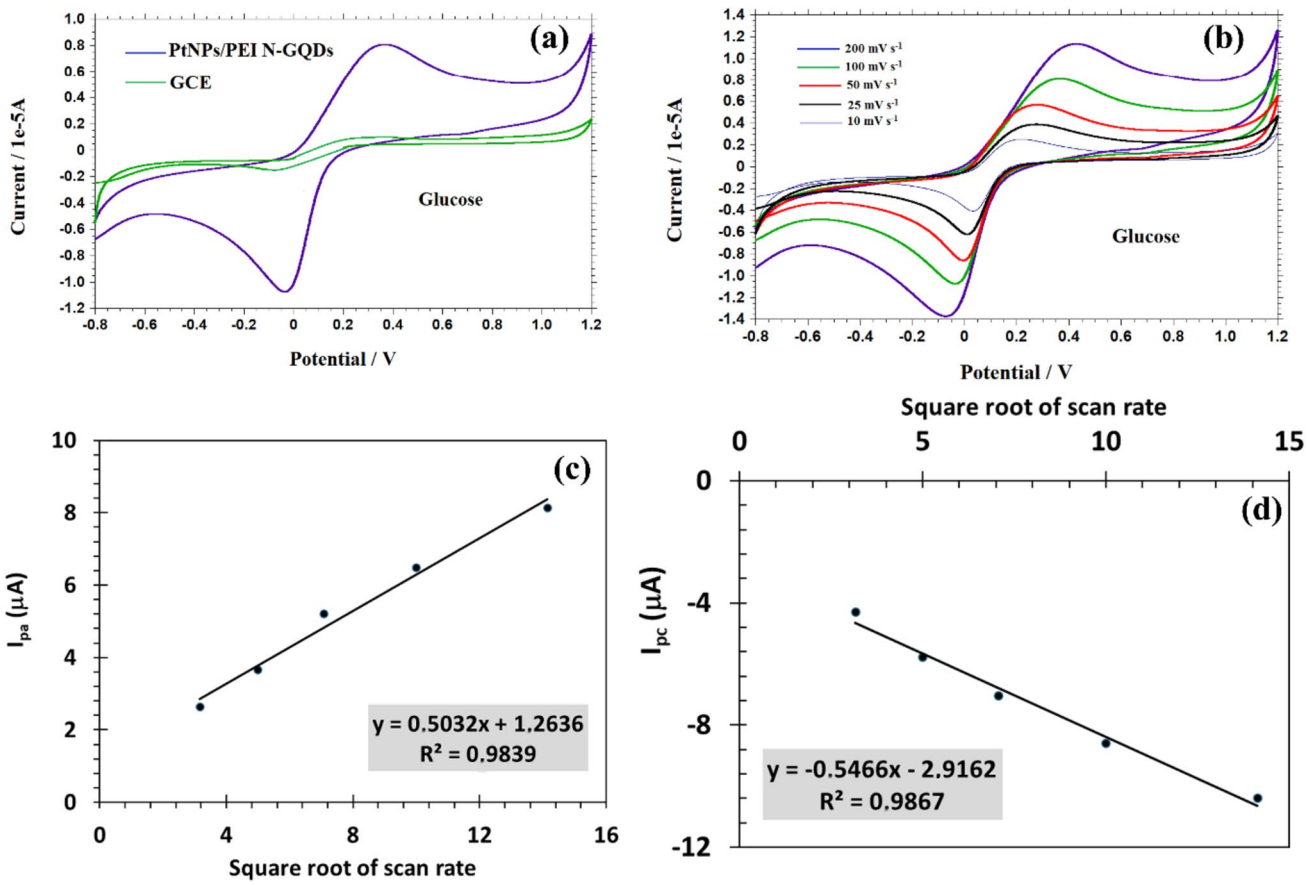

Figure 4 CV voltammograms of (**a**) 1 mM Glucose on the GC and PtNPs/PEI N-GQDs nanocomposite modified GC electrodes in 0.1 M KCl solution (pH: 7) containing 50 µM $K_3Fe(CN)_6$ and $K_4Fe(CN)_6$, **b** plots of I_{pa} versus square roots of scan rates, **c** plots of I_{pc} versus square roots of scan rates, and **d** plots of Ip_c versus square roots of scan rates.

alone. This indicates the electrocatalytic effect of the PtNPs/PEI N-GQDs nanocomposite towards glucose. Figure 4b demonstrates that increasing the square root of scan rates results in proportional increases in peak currents for both anodic and cathodic reactions. This suggests that higher scan rates correlate with increased current during these reactions. Additionally, as scan rates increase, the anodic peak shifts more positively while the cathodic peak shifts more negatively, indicating a reversible redox reaction where the electrochemical process proceeds equally in both directions. The equations relating peak currents to square roots of scan rates were determined as $I_{pa} = 0.5032x + 1.2636$ ($R^2 = 0.9839$) and $I_{pc} = -0.5466x - 2.9162$ ($R^2 = 0.9867$) for anodic and cathodic peaks, respectively (Fig. 4c and d). These findings suggest that the electro-redox reactions at the PtNPs/PEI N-GQDs nanocomposite electrode are diffusion-controlled, enhancing its electrochemical activity.

For the PtNPs/PEI N-GQDs nanocomposite-modified GC electrode, the oxidation peak for 2 µM glucose was observed at 38.80 µA at 0.068 V during differential pulse voltammetry (DPV) analysis (Fig. 5a). DPV analysis of glucose was conducted at various concentrations using the PtNPs/PEI N-GQDs nanocomposite-modified GC electrode under optimized conditions, resulting in stable and reliable oxidation peak curves, as shown in Fig. 5b. The DPV parameters included a pulse amplitude of 0.05 V, pulse time of 0.04 s, voltage step of 0.05 V, and voltage step time of 0.1 s. The PtNPs/PEI N-GQDs nanocomposite electrode exhibited excellent electrocatalytic activity for glucose sensing, generating a linear calibration curve ranging from 200 nM to 2 µM.

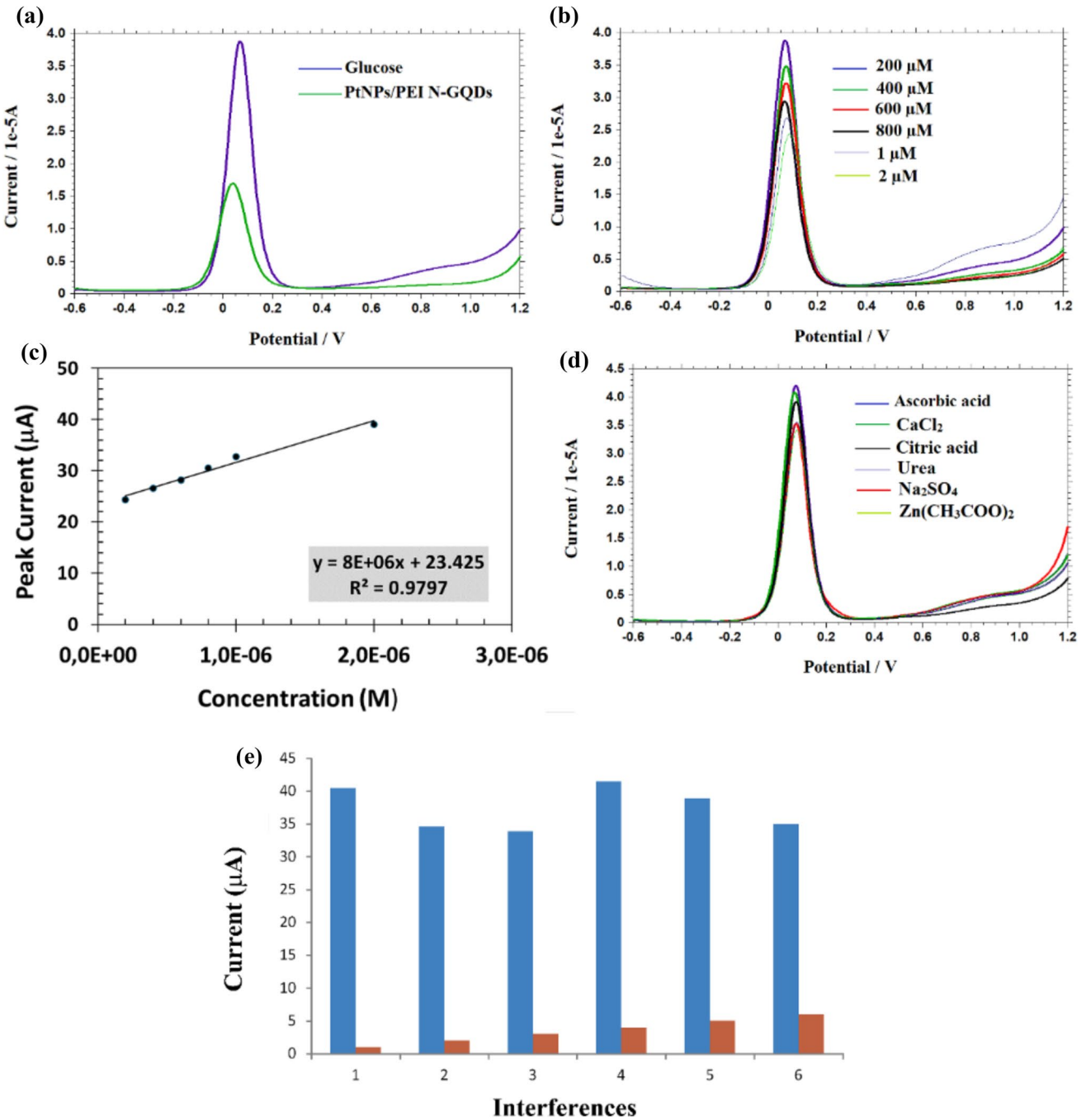

Figure 5 **a** DP voltammograms of PtNPs/PEI N-GQDs nanocomposite modified-GC electrode and 2 µM glucose at the PtNPs/PEI N-GQDs nanocomposite modified-GC electrode in 0.1 M KCl solution (pH: 7) containing 50 µM $K_3Fe(CN)_6$ and $K_4Fe(CN)_6$, **b** DP voltammograms of glucose at the PtNPs/PEI N-GQDs nanocomposite modified-GC electrode in the concentration range from 200 nM to 2 µM in 0.1 M KCl solution (pH: 7.0) containing 50 µM $K_3Fe(CN)_6$ and $K_4Fe(CN)_6$, **c** Calibration graphic of glucose, **d** electrochemical interference detection of the DP voltamograms of 2 µM Glucose in the presence of 2 µM $CaCl_2$, $Zn(CH_3COO)_2$, Na_2SO_4, ascorbic acid (AA), citric acid (CA) and urea at PtNPs/PEI N-GQDs/GC electrode in 0.1 M KCl solution (pH: 7) containing 50 µM $K_3Fe(CN)_6$ and $K_4Fe(CN)_6$, and **e** (1: $CaCl_2$, 2: $Zn(CH_3COO)_2$, 3: Na_2SO_4, 4: Ascorbic acid (AA), 5: Citric acid (CA), 6: Urea).

The DPV results further indicated robust electrocatalytic activity of the PtNPs/PEI N-GQDs nanocomposite electrode for glucose sensing, with a linear calibration equation of $I_p/\mu A = 8 \times 10^8$ ($\mu A/M$) + 23.425 and a correlation coefficient of 0.9797 (Fig. 5c). The standard deviation (s) of peak currents was used to calculate a limit of detection (LOD) of 37 nM using the formula 3 s / m (where s is the standard deviation and m is the slope of the calibration curve) [46].

Furthermore, the impact of various interfering substances—ascorbic acid (AA), citric acid (CA), urea, $CaCl_2$, $Zn(CH_3COO)_2$, Na_2SO_4—on glucose oxidation peaks was investigated using DPV (Fig. 5d and e). Solutions of these substances at 100 μM concentrations were introduced into a 0.1 M KCl electrolyte solution (pH 7) containing 100 μM glucose, 50 μM $K_3Fe(CN)_6$, and $K_4Fe(CN)_6$. The results demonstrated that these interfering substances did not affect the sensor's detection performance, highlighting its high selectivity. The electrooxidation mechanism of glucose with the PtNPs/PEI N-GQDs nanocomposite proceeds through specific chemical interactions, ensuring accurate glucose detection. The electrooxidation reaction between glucose and PtNPs/PEI N-GQDs nanocomposite proceeds as described below:

The oxidation reaction of N-GDQDs against phenols was associated with the doped pyridinic-N structure in N-GDQDs and the OH group in phenol. It was stated that phenol oxidizes to ketone under an electric field through N-GDQDs/GCE and forms a complex between N-GDQDs and phenol structure [62]. The carbonyl group of aldehydes and ketones reacts slowly with water. The acid and base are only used as catalysts to speed up the process. In our study, the polyethyleneimine group in the PtNPs/PEI N-GQDs nanocomposite first reacts with water to form polyethyleneimine-ammonium hydroxide (Reaction 1(a)). The OH^- ions, which are abundant in the medium, attack the carbonyl carbon of glucose, opening the C=O π bond, and the oxygen atom becomes negatively charged by taking an electron (Reaction 1(b)). The negatively charged oxygen takes a proton from the water,

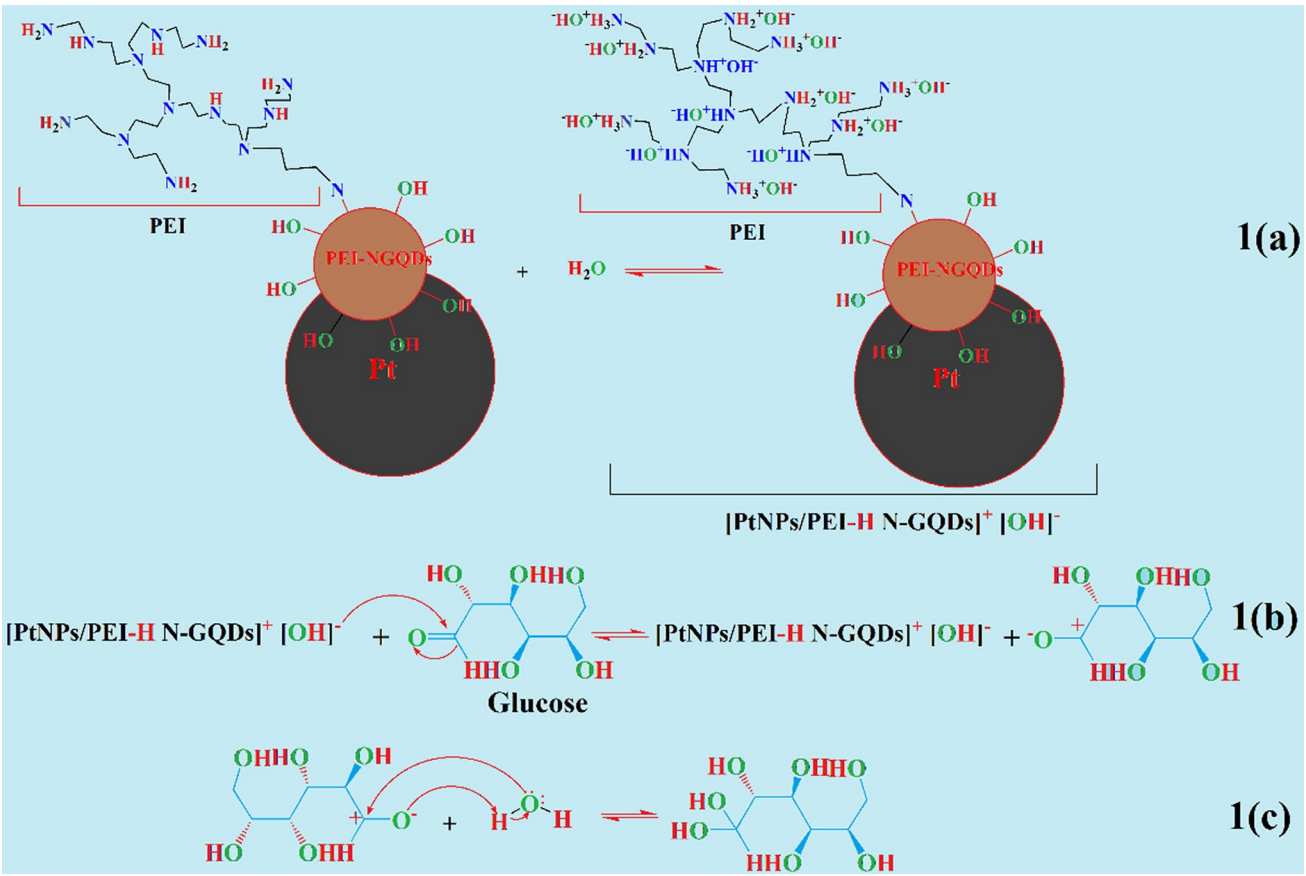

Reaction 1 (**a**), (**b**) and (**c**) between glucose and ultrasensor in aqueous media.

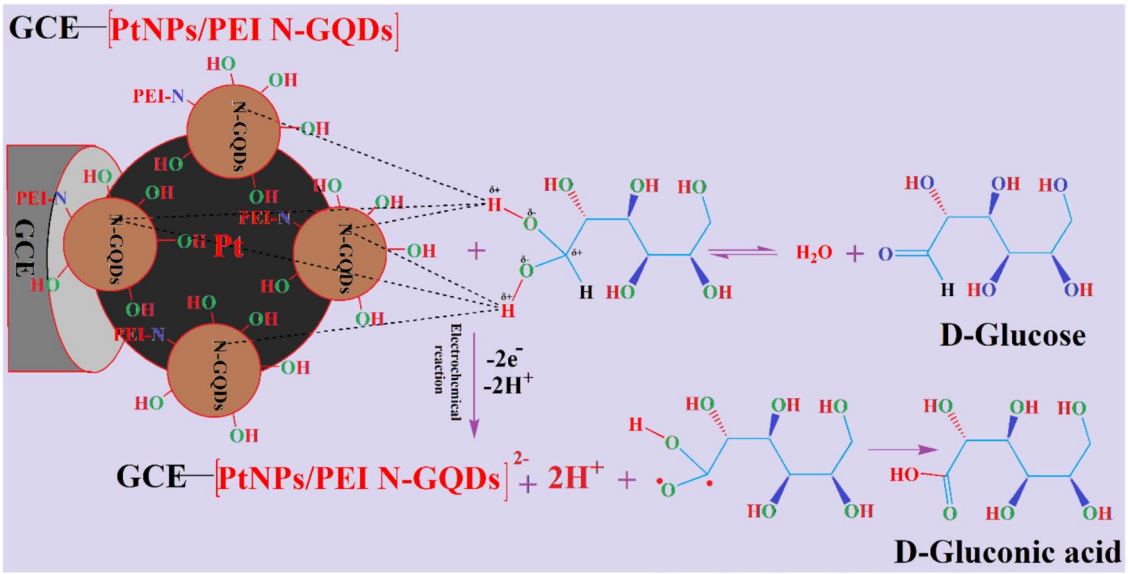

Scheme 3 Possible electrooxidation mechanism of glucose at PtNPs/PEI N-GQDs modified-GC electrode

and the geminal diol intermediate is formed (Reaction 1(c)). This intermediate forms a strong hydrogen bond with pyridinic-N at the PtNPs/PEI N-GQDs nanocomposite/GC electrode and polarizes the O–H bonds well (Scheme 3). As a result, glucose gives − $2H^+$ and − $2e^-$ to form glyconic acid radical and [PtNPs/PEI N-GQDs]2-. Finally, glyconic acid is formed by interacting glyconic oxygen and carbon radical, forming a carbon–oxygen double bond (Scheme 3).

DFT analysis

We used Gaussview software to model the PtNPs/PEI N-GQDs nanocomposite (Scheme 2, Fig. 6a) and perform geometric optimization to find its most stable configuration in the gas phase, which provides insight into its fundamental energy levels. This process helps assess the HOMO–LUMO energy gap (E_{gap}) and how it changes with different distances between PtNPs and graphene.

The optimized structure showed a minimal energy level of -3759.175 Hartree with a distance of 0.375 nm (Fig. 6a). The computed Egap was 1.14 eV, which is larger than the experimental value of 0.172 eV due to theoretical approximations and differences between vacuum conditions used in DFT calculations and the actual experimental environment, including solvent effects and temperature variations (Fig. 6b). This discrepancy is typical, as theoretical models often predict larger energy gaps compared to experimental results. The experimentally optimized structure will be used for future theoretical comparisons to refine our understanding of the nanocomposite's properties.

To enhance our study of molecular vibrations, we employed FT-IR analysis. The FT-IR spectrum (Fig. S2) confirmed the accuracy of our structural optimization by demonstrating characteristic absorption frequencies associated with various molecular vibrations. The peak transmittance in the spectrum highlights the frequencies at which the sample absorbs infrared radiation most effectively. Notable vibration bands included OH + NH2 + NH at 3740–3323 cm^{-1}, CH + CH2 at 3294–2825, C=N at 1608 cm^{-1}, C=C at 1593 cm^{-1}, C–N at 1452 cm^{-1}, and C–O at 1386 cm^{-1}. The excellent correlation between the experimental and theoretical FT-IR results validates the accuracy of our theoretical model and reinforces the reliability of our computational predictions.

FMOs consist of two essential molecular orbitals: HOMO and LUMO. The HOMO, shown by the green lines, is filled with electrons and represents the highest energy level among the occupied orbitals, acting as an electron donor. The LUMO, indicated by the red lines, remains unfilled and represents the lowest energy level among the unoccupied orbitals, functioning as an electron acceptor [63].

The energy gap between HOMO and LUMO (E_{gap}) is crucial for understanding molecular reactivity. A

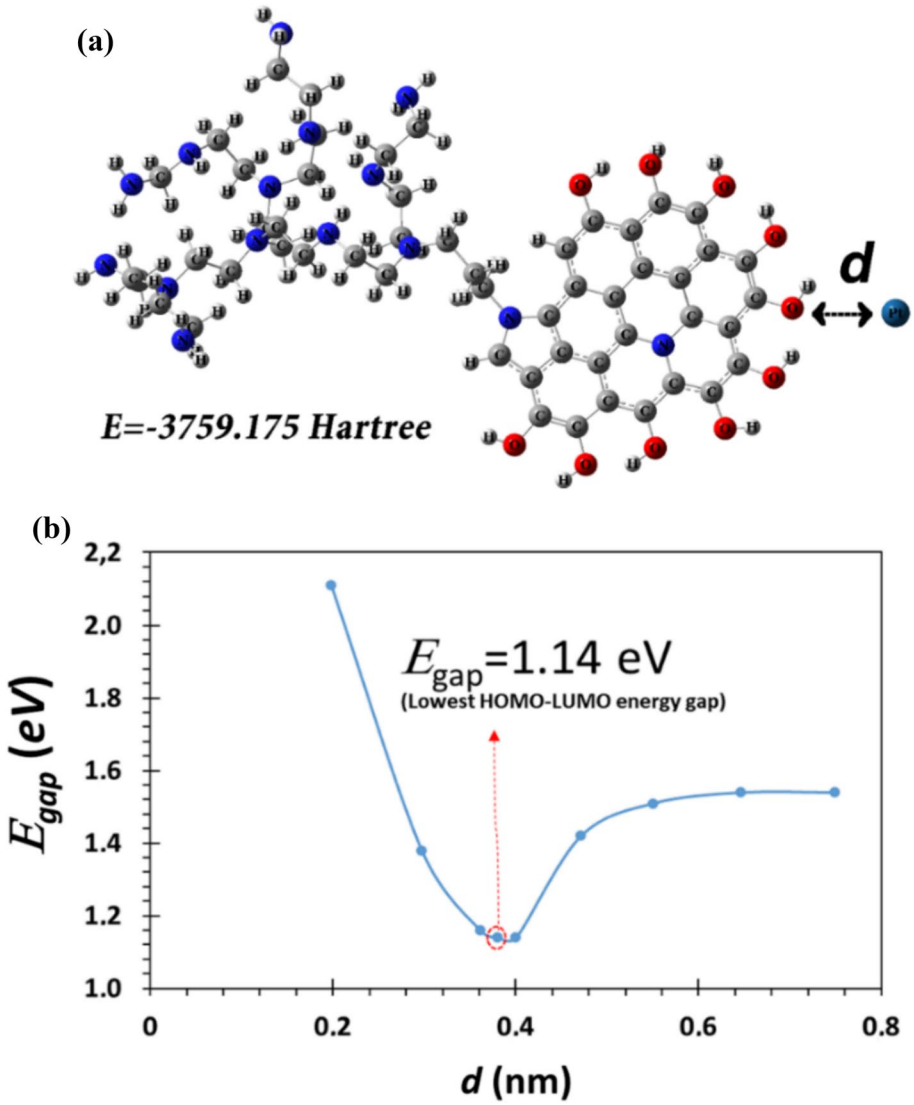

Figure 6 **a** Optimized molecular structures and **b** The variation of E_{gap} depending on the position of the Pt atom (d) in the PtNPs/PEI N-GQDs nanocomposite.

smaller Egap generally indicates higher reactivity, which can be useful for targeting specific biological molecules or pathways, such as in cancer therapies [64, 65]. This insight helps predict a molecule's propensity to engage in chemical reactions, based on the principle that chemical stability is related to electron transfer processes [61].

During chemical reactions, electrons are transferred from the HOMO to the LUMO of the reacting substances [66]. The DOS spectrum (Fig. 7a) shows that an increased HOMO peak suggests a higher potential for chemical interaction. For the PtNPs/PEI N-GQDs nanocomposite, the enhanced HOMO peak correlates with increased chemical interaction potential, affecting biological outcomes like cytotoxicity and apoptosis in ovarian cancer cells.

A molecule with a small E_{gap} is also more likely to engage in redox reactions, which is advantageous for treatments based on oxidative stress, such as certain cancer therapies [67]. This enhances the molecule's stability, which is critical for improving binding affinity and advancing drug design. The E_{gap} value of 1.14 eV for the PtNPs/PEI N-GQDs nanocomposite (Fig. 7b) indicates its advantageous reactivity. Proper alignment of the HOMO of the nanocomposite with the LUMO of the target molecule is crucial for effective drug design and targeting [13]. Examining the isosurfaces of HOMO and LUMO provides valuable insights into electronic structure and reactivity. The HOMO isosurface shows areas of high electron density that are susceptible to nucleophilic attack, essential for understanding drug interactions [68, 69]. The LUMO

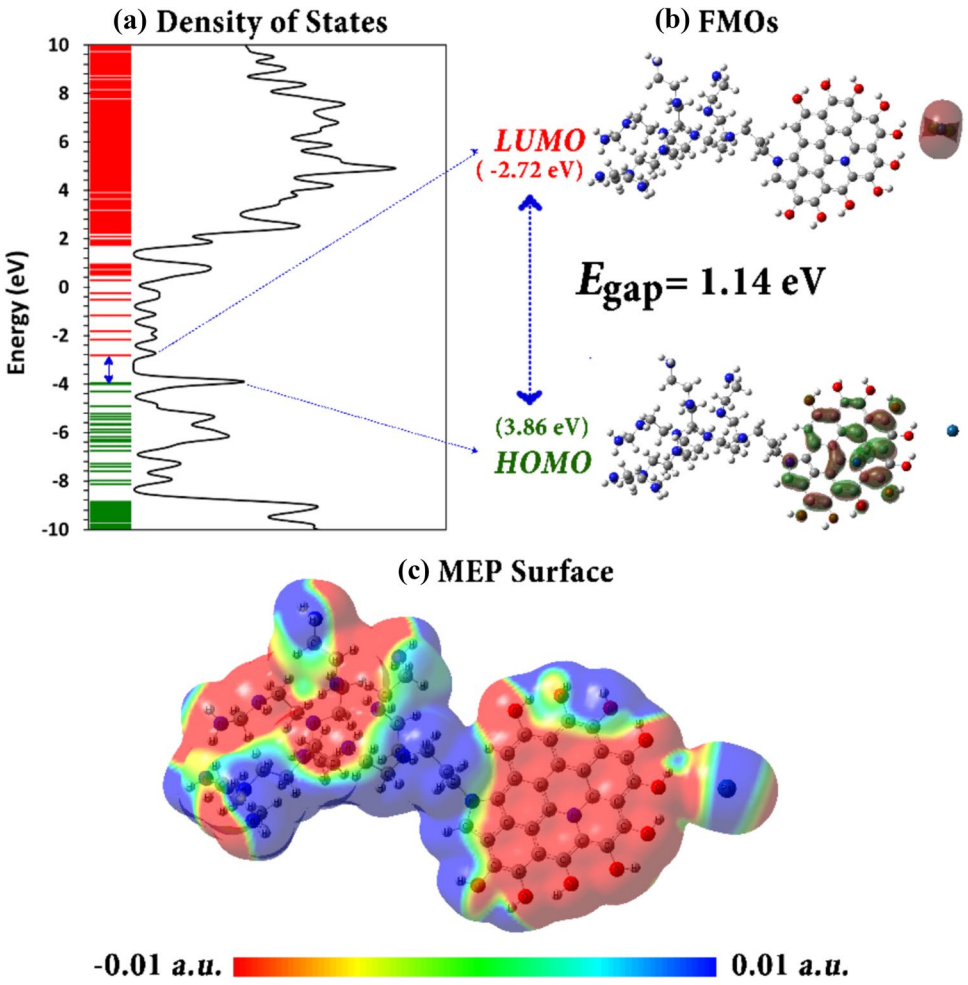

Figure 7 **a** DOS spectrum, **b** FMOs and **c** MEP surface of PtNPs/PEI N-GQDs nanocomposite.

isosurface reveals electron-deficient regions, indicating sites prone to nucleophilic attack. This information helps assess the stability and potential toxicity of molecules. The DOS spectrum's peaks suggest higher densities of electronic states at specific energy levels, associated with interactions with biological systems. The peaks in HOMOs indicate available electrons for chemical interactions, while peaks in LUMOs represent electron vacancies capable of redox reactions [66].

The method for identifying reactive sites in a molecule involves analyzing the Molecular Electrostatic Potential (MEP) [13]. This technique maps the distribution of electric charge across a nanocomposite, highlighting regions prone to electrophilic (electron-withdrawing) or nucleophilic (electron-donating) attacks. MEP surfaces use color gradients to represent reactivity: blue for nucleophilic regions, green for neutral areas, and red/yellow for electrophilic regions. Red areas indicate high electron density, suggesting electrophilic sites, while blue areas denote nucleophilic sites [70]. For example, platinum (Pt) interacting with OH groups can both donate and accept electron density, displaying mixed electrophilic and nucleophilic behavior. Understanding these interactions is crucial for predicting molecular reactivity and designing drugs or other compounds for specific applications, such as targeted drug delivery or cancer treatment.

Furthermore, we conducted a theoretical examination of the UV–Vis spectra for the compounds when dissolved in aqueous solutions. This thorough analysis explored various spectroscopic characteristics related to electronic transitions, including absorption wavelengths, excitation energies, and significant transitions. All these factors were meticulously considered and are documented in Table 1, which includes the highest oscillator strength [71]. Table 1 clearly illustrates the absorption peaks indicating three major transitions at 347 nm (H-22 to LUMO, H-12 to L + 2 and H-7 to L + 3 with contributions of 37%, 14%, and 25%, respectively), three

Table 1 Optical properties of PtNPs/PEI N-GQDs nanocomposite in water media

Compound	Experimental	Theoretical			
	λ_{abs} (nm)	λ_{abs} (nm)	Excitation Energy (eV)	Oscillator Strength f	Major Transitions
PtNPs/PEI N-GQDs	357	347	3.58	0.41	H-22 → LUMO (37%) H-12 → L + 2 (14%) H-7 → L + 3 (25%)
	271	271	4.58	0.26	H-23 → L + 1 (34%) H-12 → L + 4 (21%) H-5 → L + 9 (20%)
	251	249	4.98	0.25	H-23 → L + 2 (15%) H-22 → L + 3 (37%) H-6 → L + 6 (13%)

Table 2 IC_{50} values of PtNPs/PEI N-GQDs nanocomposite in OVCAR-3 cell line

Nanocomposite	IC_{50} (μg/μL) ± S.D
PtNPs/PEI N-GQDs	10.05 ± 1.124

major transitions at 271 nm (H-23 to L + 1, H-12 to L + 4, and H-5 to L + 9 with contributions of 34%, 21%, and 20%, respectively), and three major transitions at 249 nm (H-23 to L + 2, H-22 to L + 3 and H-6 to L + 6 with contributions of 15%, 37% and 13%, respectively). These transitions possess excitation energies of 3.58, 4.58 eV, and 4.98 eV, respectively. Importantly, the UV–Vis findings closely correlate with the experimental data outlined in Table 1.

Effect of PtNPs/PEI N-GQDs nanocomposite on the proliferation of OVCAR-3 cells

Cell viability tests are commonly used to evaluate whether molecules affect cell proliferation or induce cell death. In this study, the MTT assay was utilized to assess the anti-proliferative effects of PEI-functionalized N-GQDs loaded with Pt nanoparticles on OVCAR-3 ovarian cancer cells. The cytotoxicity was determined by calculating the IC_{50}, which was found to be 10.05 ± 1.124 μg/μL. The results, shown in Table 2 and Fig. 8, indicated significant cytotoxicity with effects observed across a dose range of 0.24 μg/μL to 500 μg/μL ($p < 0.001$). This nanocomposite demonstrated strong cytotoxicity even at lower doses compared to cisplatin, a standard chemotherapy drug. This increased efficacy is attributed to the nanocomposite's ability to enhance cellular permeability,

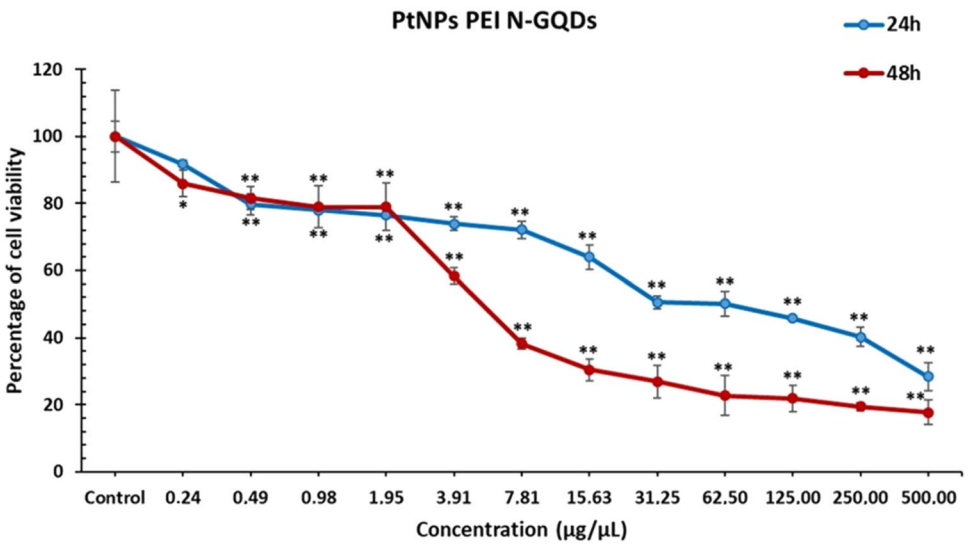

Figure 8 Effects of PtNPs/PEI N-GQDs (0,24–500 μg/μl) on the viability of OVCAR-3 cells (*$p < 0.05$ and ** $p < 0.001$ show significant differences from the control group).

thereby boosting the interaction of Pt with DNA inside the cells [72–78].

Induction of apoptosis in OVCAR-3 cells by PtNPs/PEI N-GQDs

Conventional chemotherapy is the primary treatment for cancer and is often combined with surgery and radiotherapy. Research into anti-cancer mechanisms targets various processes, including inhibition of cell viability, induction of apoptosis, inhibition of cell proliferation, modulation of signal transduction pathways, and induction of cell cycle arrest [72, 73]. In our study, flow cytometric analysis was used to evaluate whether PtNPs/PEI N-GQDs induce apoptosis in OVCAR-3 cells.

The results showed that PtNPs/PEI N-GQDs treatment significantly reduced the viable cell rate to 45.85% ($p < 0.05$) compared to controls, with increased early (22.65%) and late apoptotic cells (29.95%) ($p < 0.05$) observed after 48 h (Fig. 9a and b). The rate of necrosis was low at 1.55% ($p > 0.05$). These findings align with Qin et al.'s discovery that GQDs induce apoptosis via a mitochondria-associated pathway [74].

Studies on GQDs that focus on their antiproliferative and anticancer characteristics show that these substances can enter cells and interact with proteins, RNA, and DNA to cause cytotoxicity. At the same time, intracellular ROS produced by mitochondria increases in cells treated with graphene. The cell eventually undergoes apoptosis and dies due to the metabolic activities set off by this rise in ROS levels, moving from the mitochondria to the cytoplasm [75, 79, 80]. Therefore, in accordance with the data from the literature, we suggest that adding PtNP to PEI N-GQDs in our investigation increased apoptosis by up to 52.8% via enhancing ROS generation from mitochondria.

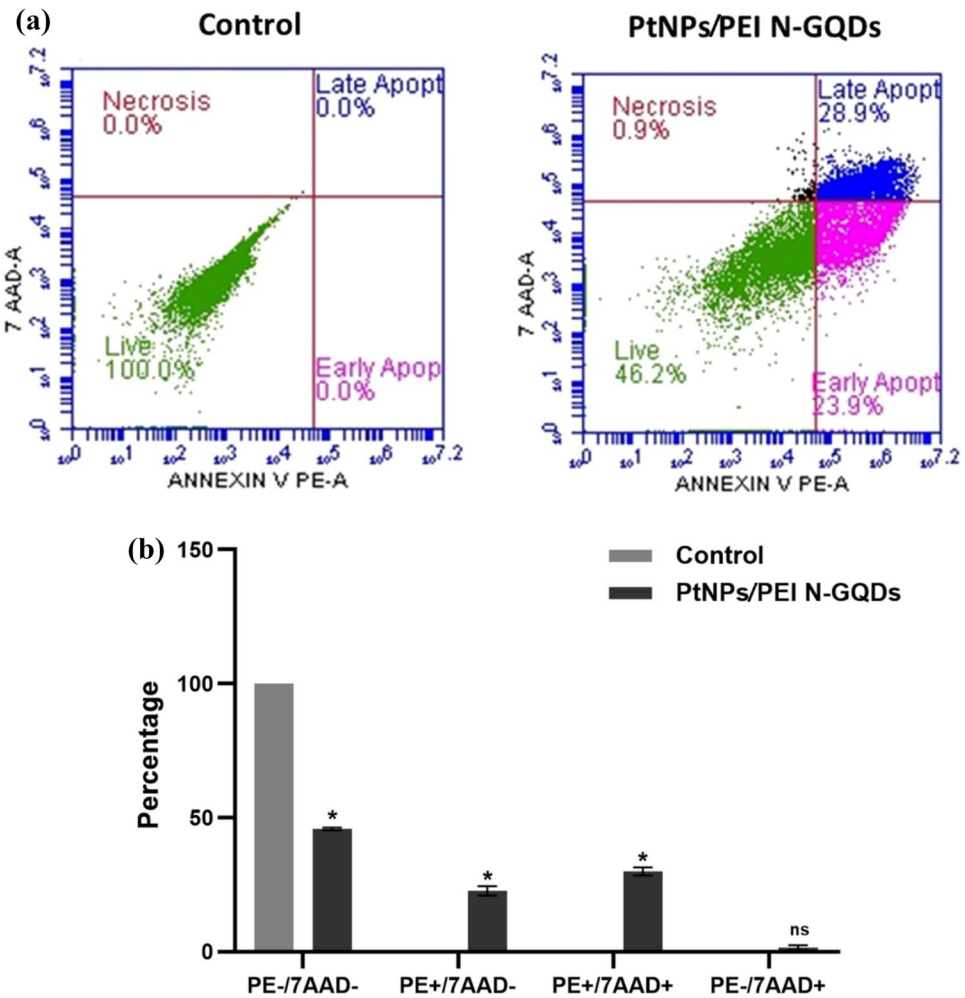

Figure 9 PtNPs/PEI N-GQDs induce apoptosis in vitro. Flow cytometric analysis of OVCAR-3 cells stained with Annexin V PE/7-AAD for 48 h (**a**) Flow cytometry results are represented as dot Plots. **b** Flow cytometry results of OVCAR-3 cells with/without PtNPs/PEI N-GQDs were shown as bar graphs. Control; Viability of distilled water (without PtNPs/PEI N-GQDs) treated cells was considered as 100%. Viable cells (PE-/7AAD-); early apoptotic cells (PE + /7AAD-), late apoptotic cells (PE + /7AAD +) and necrotic cells (PE-/7AAD +) (* $p < 0.05$ shows significant differences from the control and other groups).

PtNPs/PEI N-GQDs induces cell cycle arrest in OVCAR-3 cells

The cell cycle and apoptosis are critical for regulating cell growth and maintaining genomic integrity. Checkpoints within the cell cycle prevent cells with DNA damage from continuing to divide, either by repairing the damage or by undergoing apoptosis [76, 77]. Cyclin-dependent kinase inhibitors (CKIs) help manage cellular growth by regulating progression through cell cycle phases. Damaged DNA can cause cells to halt the cycle or initiate apoptosis to avoid the replication of irreparably damaged chromosomes [13, 78].

In our study, flow cytometry was used to assess how PtNPs/PEI N-GQDs affect the cell cycle distribution of OVCAR-3 cells. We observed that PtNPs/PEI N-GQDs caused a significant increase in the proportion of cells in the G0/G1 phase, from 78.2% to 94.9% ($p < 0.001$), with a concurrent decrease in the S and G2/M phases ($p < 0.001$) [81]. This suggests that PtNPs/PEI N-GQDs induce cell cycle arrest at the G0/G1 checkpoint (see Fig. 10a and b).

Previous research [13] supports these findings: p53 and Cyclin-CDK complexes are crucial in responding to DNA damage by halting the cell cycle [82]. Studies have shown that Pt-based drugs can arrest cells at various checkpoints, including sub-G0/G1, S, or G2/M phases [83, 84]. Our study, which demonstrates that PtNPs/PEI N-GQDs cause G0/G1 phase arrest in ovarian cancer cells, is the first to report this specific effect. This aligns with findings from Tian et al., who noted that GQDs induce DNA damage responses, and Ku et al., who observed G2/M checkpoint arrest with GQDs in breast cancer cells [85, 86]. This study highlights that PtNPs/PEI N-GQDs contribute to cell cycle arrest at G0/G1 through genotoxic damage rather than just DNA fragmentation.

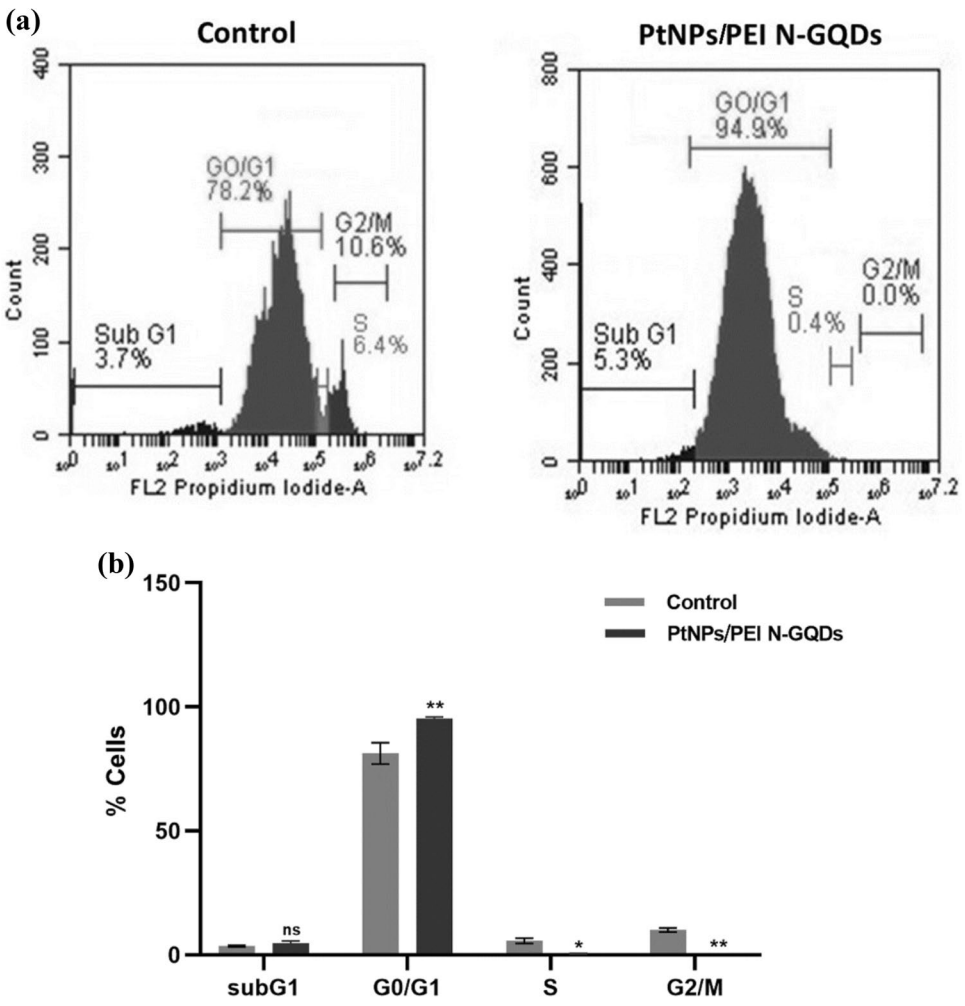

Figure 10 (**a**) Cell cycle analysis of OVCAR-3 cells treated with PtNPs/PEI N-GQDs was determined by flow cytometry after staining with PI for 48 h; (**b**) Percentages of each cell cycle phase were obtained by flow cytometric analysis (* $p < 0.05$ and ** $p < 0.001$ show significant differences from the control group).

Anti-angiogenic effects of PtNPs/PEI N-GQDs nanocomposite

In cancer research, the "3Rs" (reduce, refine, replace) emphasize the need for alternative models in toxicity studies. The chicken egg model, particularly the CAM (chorioallantoic membrane) assay, has gained prominence in toxicological and cancer research due to its ability to investigate molecular mechanisms of anticancer drugs [87]. The CAM, a vascularized membrane in developing chicken embryos, aids studies of angiogenesis, tumor cell invasion, and metastasis by providing a rich network of blood vessels [88, 89].

In our study, the ex ovo CAM assay was used to evaluate the angiogenic effects of PtNPs/PEI N-GQDs. Chick CAMs were treated with PtNPs/PEI N-GQDs (10.05 µg/50 µL) and vascular density was measured at 0, 24, and 48 h. The results showed a significant reduction in vascular proliferation to 5.293% at 24 h and 8.357% at 48 h compared to the control group ($p < 0.05$) [55] (Fig. 11a and b). This study demonstrates that PtNPs/PEI N-GQDs significantly reduce vascular density in the CAM, supporting their potential as anti-angiogenic agents. Zhao et al. [90] also found that GQDs can serve as biocompatible anti-angiogenic nanomedicines, further validating the use of PtNPs/PEI N-GQDs in targeting angiogenesis.

Conclusion

In this study, PtNPs/PEI N-GQDs nanocomposite was synthesized using a one-step hydrothermal method and characterized. The modified glassy carbon electrode (GCE) with PtNPs/PEI N-GQDs was analyzed electrochemically using cyclic voltammetry (CV). The band gap energy and HOMO–LUMO levels were found to be 0.172 eV, -4.991 eV, and -5.163 eV, respectively, indicating high conductivity. The specific capacitance was measured at 1.008 F/g. The electrode

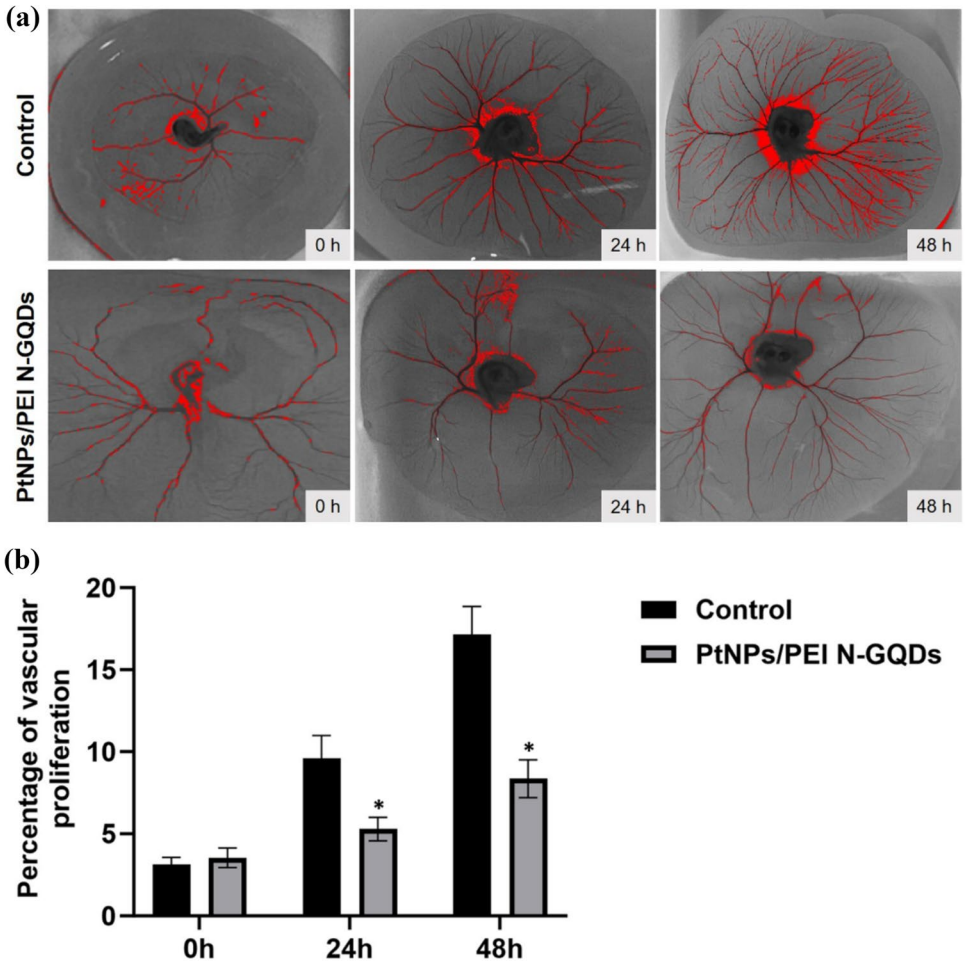

Figure 11 Ex ovo CAM angiogenesis assay. **a** Photographs of the CAM treated with PtNPs/PEI N-GQDs and control (untreated), **b** Graphical representation of vascular proliferation levels in control and treated with PtNPs/PEI N-GQDs. (* $p < 0.05$ shows significant differences from the control group).

showed excellent electrocatalytic activity for glucose sensing, with a linear calibration range from 200 nM to 2 μM and high selectivity even in the presence of interfering substances. The sensor's performance suggests potential applications in detecting and monitoring cancers like pancreatic and ovarian cancer. Additionally, the PtNPs/PEI N-GQDs demonstrated anti-cancer properties, including significant cytotoxic effects on ovarian cancer cells, inhibition of angiogenesis, and induction of apoptosis. These results suggest the nanocomposite could be a promising candidate for cancer treatment, potentially preventing or delaying tumor metastasis.

Acknowledgements

This work was supported by Ankara University Scientific Research Projects Coordination Unit (Grant number: FBA-2024-3174). The numerical calculations reported in this paper were fully performed at TUBITAK ULAKBIM, High Performance and Grid Computing Center (TRUBA resources). XPS and TEM analyses were performed at METU Central Laboratory.

Author contributions

BAG: conceptualization, data curation, formal analysis, investigation, visualization, writing – original draft, writing – review & editing; OFK: conceptualization, data curation, formal analysis, investigation, visualization; MK: conceptualization, data curation, formal analysis, investigation, visualization, writing – original draft; DK: investigation, visualization, project administration, writing – original draft, writing – review & editing; AA: investigation, resources, visualization; SYK: formal analysis, investigation, resources, visualization; AK: formal analysis, investigation, resources, visualization; IK: resources, writing – review & editing; AS: resources, writing – review & editing; NOY: investigation, resources; TO: resources, writing – review & editing; EKS: resources, writing – review & editing; BB: conceptualization, data curation, formal analysis, investigation, visualization, project administration, supervision, writing – original draft, writing – review & editing; HU: formal analysis, investigation, visualization, project administration, supervision, writing – review & editing; MY: conceptualization, data curation, formal analysis, investigation, project administration, visualization, supervision, writing – original draft, writing – review & editing.

Funding

Open access funding provided by the Scientific and Technological Research Council of Türkiye (TÜBİTAK).

Data availability

Not applicable.

Declarations

Conflict of interest The authors declare no competing financial interest.

Ethical approval Not applicable.

Supplementary Information The online version contains supplementary material available at https://doi.org/10.1007/s10853-025-10722-y.

References

[1] Liu H, Liu Y, Zhu D (2011) J Mater Chem 21:3335–3345

[2] Ma L, Hu H, Zhu L, Wang J (2011) The Journal of Physical Chemistry C 115:6195–6199
[3] Gong K, Du F, Xia Z, Durstock M, Dai L (2009) science 323: 760–764.
[4] Cervantes-Sodi F, Csányi G, Piscanec S, Ferrari AC (2008) Phys Rev B 77:165427
[5] Deifallah M, McMillan PF, Corà F (2008) The Journal of Physical Chemistry C 112:5447–5453
[6] Lherbier A, Blase X, Niquet Y-M, Triozon F, Roche S (2008) Phys Rev Lett 101:036808
[7] Li Y, Zhou Z, Shen P, Chen Z (2012) The Journal of Physical Chemistry C 116:208–213
[8] Kaur M, Kaur M, Sharma VK (2018) Adv Coll Interface Sci 259:44–64
[9] Michos FI, Chronis AG, Sigalas MM (2023) Nanomaterials 13:2589
[10] Ghaffarkhah A, Hosseini E, Kamkar M et al (2022) Small 18:2102683
[11] Lu W, Shen N, Celia C, Xie Y, Chang Q, Deng X (2023) New J Chem 47:20966–20975
[12] Xu Q, Li C, Meng X, Duo X, Feng Y (2024) Regenerative Biomaterials 11: rbae013.
[13] Gunes BA, Kirlangic OF, Kilic M et al (2024) ACS Omega 9:13342–13358. https://doi.org/10.1021/acsomega.3c10324
[14] Biswas MC, Islam MT, Nandy PK, Hossain MM (2021) ACS Materials Letters 3:889–911
[15] Wang L, Wu B, Li W et al (2018) Advanced Biosystems 2:1700191
[16] Lo P-Y, Lee G-Y, Zheng J-H, Huang J-H, Cho E-C, Lee K-C (2020) ACS Appl Bio Mater 3:5948–5956
[17] Raghavan A, Radhakrishnan M, Soren K et al (2023) ACS Appl Bio Mater 6:2237–2247
[18] Facure MH, Schneider R, Lima JB, Mercante LA, Correa DS (2021) Electrochem 2:490–519
[19] Bai Q, Luo H, Yi X et al (2022) Microchem J 179:107521
[20] Kondo T, Horitani M, Yuasa M (2012) International Journal of Electrochemistry 2012.
[21] Gao J, He S, Nag A (2021) Sensors 21:2818
[22] Zhang S, Li Y, Song H et al (2016) Sci Rep 6:19292
[23] Gong X, Yang J, Yao K, et al. (2023).
[24] Li Y, Zhao Y, Cheng H et al (2012) J Am Chem Soc 134:15–18
[25] Calabro RL, Yang D-S, Kim DY (2019) ACS Applied Nano Materials 2:6948–6959
[26] Xue Z, Gao H, Li X (2018) Dyes Pigm 156:379–385
[27] Qu D, Zheng M, Zhang L et al (2014) Sci Rep 4:5294
[28] Jin L, Wang Y, Yan F, Zhang J, Zhong F (2019) Journal of Nanomaterials 2019.
[29] Lin L, Rong M, Lu S et al (2015) Nanoscale 7:1872–1878
[30] Wang J, Lu C, Chen T et al (2019) Nanophotonics 9:3831–3839
[31] Malahom N, Ma-In T, Naksen P et al (2023) ACS Applied Nano Materials 6:11144–11153
[32] Orhan E, Anter A, Ulusoy M et al (2023) Advanced Electronic Materials 9:2300261
[33] Berktaş Z, Yıldız M, Seven E, Orhan EO, Altındal Ş (2022) FlatChem 36:100436
[34] Berktas Z, Orhan E, Ulusoy M, Yildiz M (2023) Altındal Se. ACS Appl Electron Mater 5:1804–1811
[35] Şenel B, Demir N, Büyükköroğlu G, Yıldız M (2019) Saudi Pharmaceutical Journal 27:846–858
[36] Karatay A, Erdener D, Gürcan C et al (2022) J Photochem Photobiol, A 426:113741
[37] Dong Y, Shao J, Chen C et al (2012) Carbon 50:4738–4743
[38] Permatasari FA, Aimon AH, Iskandar F, Ogi T, Okuyama K (2016) Sci Rep 6:21042
[39] Yan F, Sun Z, Zhang H, Sun X, Jiang Y, Bai Z (2019) Microchim Acta 186:1–37
[40] He S, Turnbull MJ, Nie Y, Sun X, Ding Z (2018) Surf Sci 676:51–55
[41] Kim BG, Ma X, Chen C et al (2013) Adv Func Mater 23:439–445
[42] Qin Y (2016) University of South Florida,
[43] Frieler M, Pho C, Lee BH, Dobrovolny H, Akkaraju GR, Naumov AV (2021) Nanomaterials (Basel) 11. https://doi.org/10.3390/nano11010140
[44] Fan HY, Yu XH, Wang K et al (2019) Eur J Med Chem 182:111620. https://doi.org/10.1016/j.ejmech.2019.111620
[45] Song M, Cui M, Liu K (2022) Eur J Med Chem 232:114205. https://doi.org/10.1016/j.ejmech.2022.114205
[46] Yağmur Kabaş S (2024) J Electroanal Chem 964:118316. https://doi.org/10.1016/j.jelechem.2024.118316
[47] Roy LE, Hay PJ, Martin RL (2008) J Chem Theory Comput 4:1029–1031
[48] Check CE, Faust TO, Bailey JM, Wright BJ, Gilbert TM, Sunderlin LS (2001) J Phys Chem A 105:8111–8116
[49] Frisch M, Trucks G, Schlegel H, et al. (2010) Inc.: Wallingford, CT.
[50] Dennington R, Keith T, Millam J (2009).
[51] O'boyle NM, Tenderholt AL, Langner KM (2008) Journal of computational chemistry 29: 839–845.
[52] Runge E, Gross EK (1984) Phys Rev Lett 52:997
[53] Ozkan T, Hekmatshoar Y, Karabay AZ, et al. (2021) Leukemia Res 102. https://doi.org/10.1016/j.leukres.2021.106523
[54] Dohle DS, Pasa SD, Gustmann S et al (2009). J Vis Exp. https://doi.org/10.3791/1620

[55] Shereema RM, Sruthi TV, Kumar VBS, Rao TP, Shankar SS (2015) Biochemistry-Us 54:6352–6356. https://doi.org/10.1021/acs.biochem.5b00781
[56] Rocha APdM, Alayo MI, da Silva DM (2022) Applied Sciences 12: 8686.
[57] Bian Y, He B, Li J (2016) BioResources 11:6299–6308
[58] Chen M-L, Park C-Y, Choi J-G, Oh W-C (2011) J Korean Ceram Soc 48:147–151
[59] Holzwarth U, Gibson N (2011) Nat Nanotechnol 6:534–534
[60] Bayat A, Saievar-Iranizad E (2017) J Lumin 192:180–183
[61] Bouzina A, Bouone YO, Sekiou O et al (2023) RSC Adv 13:19567–19584
[62] Manbohi A, Ahmadi SH (2019) Sensing and Bio-Sensing Research 23:100270
[63] Politzer P, Abu-Awwad F (1998) Theoret Chem Acc 99:83–87. https://doi.org/10.1007/s002140050307
[64] Fong CW (2019) Eigenenergy, Adelaide, Australia,
[65] Yasir HM, Hanoon FH (2020) IOP Conference Series: Materials Science and EngineeringIOP Publishing,
[66] Han Mİ, Dengiz C, Doğan ŞD, Gündüz MG, Köprü S, Özkul C (2022) J Mol Struct 1252:132007. https://doi.org/10.1016/j.molstruc.2021.132007
[67] Ashfaq M, Ali A, Tahir MN, Kuznetsov A, Munawar KS, Muhammad S (2022) J Mol Struct 1262:133088. https://doi.org/10.1016/j.molstruc.2022.133088
[68] Devasia J, Chinnam S, Khatana K et al (2023) Polycyclic Aromat Compd 43:1941–1956
[69] Abdallah MAB (2018) J Mol Struct 1171:76–86
[70] Pourjavadi A, Doroudian M, Bagherifard M, Bahmanpour M (2020) New J Chem 44:17302–17312
[71] Ruger R, Van Lenthe E, Lu Y, Frenzel J, Heine T, Visscher L (2015) J Chem Theory Comput 11:157–167
[72] Bakshi H, Sam S, Rozati R et al (2010) Asian Pac J Cancer Prev 11:675–679
[73] Rauf A, Abu-Izneid T, Khalil AA, et al. (2021) Molecules 26. https://doi.org/10.3390/molecules26237368
[74] Qin Y, Zhou Z-W, Pan S-T et al (2015) Toxicology 327:62–76
[75] Ou L, Lin S, Song B, Liu J, Lai R, Shao L (2017) International journal of nanomedicine: 6633–6646.
[76] Matthews HK, Bertoli C, de Bruin RAM (2022) Nat Rev Mol Cell Biol 23:74–88. https://doi.org/10.1038/s41580-021-00404-3
[77] Kwan YP, Saito T, Ibrahim D et al (2016) Pharm Biol 54:1223–1236. https://doi.org/10.3109/13880209.2015.1064451
[78] Arora S, Tandon S (2015) Homeopathy 104:36–47
[79] Jiang D, Chen Y, Li N et al (2015) PLoS ONE 10:e0144906
[80] Ramachandran P, Khor B-K, Lee CY et al (2022) Biomedicines 10:421
[81] Plesca D, Mazumder S, Almasan A (2008) Methods Enzymol 446:107–122
[82] Ngabire D, Seong Y, Patil MP, Niyonizigiye I, Seo YB, Kim G-D (2018) Int J Oncol 53:2300–2308
[83] Swift L, Golsteyn R (2016) Genome StabilityElsevier,
[84] Velma V, Dasari SR, Tchounwou PB (2016) Biomarker insights 11: BMI. S39445.
[85] Tian X, Xiao B-B, Wu A et al (2016) Toxicology research 5:1639–1648
[86] Ku T-H, Shen W-T, Hsieh C-T, Chen GS, Shia W-C (2023) Int J Mol Sci 24:4046
[87] Buhr CR, Wiesmann N, Tanner RC, Brieger J, Eckrich J (2020) Nanomaterials 10. https://doi.org/10.3390/nano10122328
[88] Schäfer-Korting M, Stuchi Maria-Engler S, Landsiedel R (2021) Organotypic models in drug development. Springer Nature, Cham
[89] Liu Y, Luo Y, Cai M et al (2021) Indian J Med Res 154:680–690. https://doi.org/10.4103/ijmr.IJMR_1160_19
[90] Zhao N, Gui X, Fang Q et al (2022) J Nanobiotechnology 20:174. https://doi.org/10.1186/s12951-022-01362-4